doi:10.1038/nature11202

Swirl no.	Diameter (arcsec)	Lifetime (seconds)	SDO 304	SDO 171	SDO 193	SDO 211
#1	4.0	708	☑	☑	-	-
#2	3.5	876	☑	-	-	-
#3	3.5	936	☑	☑	☑	☑
#4	3.0	1,140	☑	☑	☑	-
#5	3.5	792	☑	☑	-	-
#6	3.0	852	☑	☑	-	-
#7	2.0	996	☑	☑	☑	☑
#8	4.0	540	☑	-	-	-
#9	5.5	396	☑	-	-	-
#10	5.0	852	☑	☑	☑	☑
#11	7.5	732	☑	☑	☑	☑
#12	5.0	1,032	☑	☑	-	-
#13	3.0	410	☑	☑	-	-
#14	3.5	420	☑	-	-	-

Supplementary Table 1: Swirl statistics. A total number of 14 chromospheric swirls is detected in the observational data set from May 8th, 2011 (Figs. 1, 2). The properties of the individual swirls vary. The table contains the determined diameters and lifetimes for each swirl. Based on the 14 detections, we derive diameters of (4.0 ± 1.4) arcsec or (2,900 ± 1,000) km and lifetimes of (12.7 ± 4.0) min. The 4 rightmost columns specify in which SDO/AIA channel a corresponding signal was present. All cases are identified in the channel at 30.4 nm (SDO 304), whereas 4 events show a signal in all 4 analysed SDO channels. These observations prove that (i) swirls and the connected small-scale tornadoes are ubiquitous in the solar atmosphere and (ii) extend into the transition region and corona.

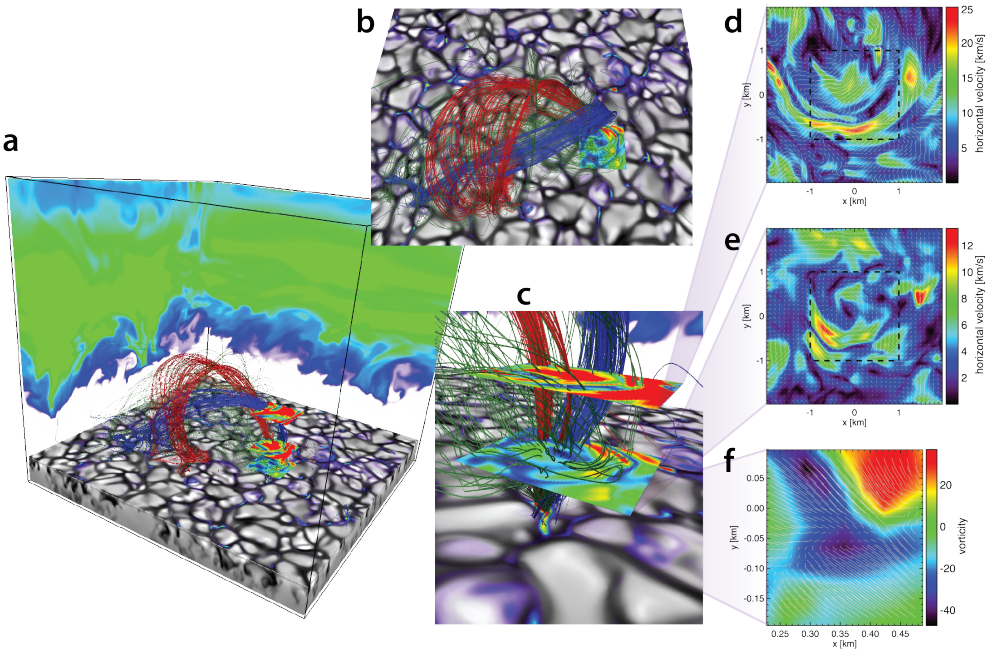

Supplementary Figure S1: Magnetic field structure expanding into the corona. This snapshot from a numerical simulation with Bifrost[22] shows a magnetic loop that exhibits a swirl signature. The computational box **(a)** has a spatial extent of 16.6 Mm × 16.6 Mm × 15.4 Mm and stretches from the top of the convection zone into the corona. The model contains a large loop structure (**b**, seen from above) that connects groups of photospheric footpoints with opposite polarity a few 1000 km apart and protrudes into the low corona. There is a swirl located above one of the magnetic footpoints **(c)**. The swirl can be seen in horizontal cross-sections at heights of, e.g., z = 2,000 km **(d)** and z = 1,000 km **(e)**. Part of the photospheric footpoint coincides with a vortex flow and a region of high negative vorticity **(f)**, causing a progressive twisting of the loop. The 3-D visualisations (constructed with VAPOR[30]) contain images of the granulation at the surface (grey), the gas temperature (coloured slices at the back), and three sets of magnetic field lines. The field lines start from seeds at different heights (green: z = 0 km, red z = 2,000 km, blue z = 4,000 km).

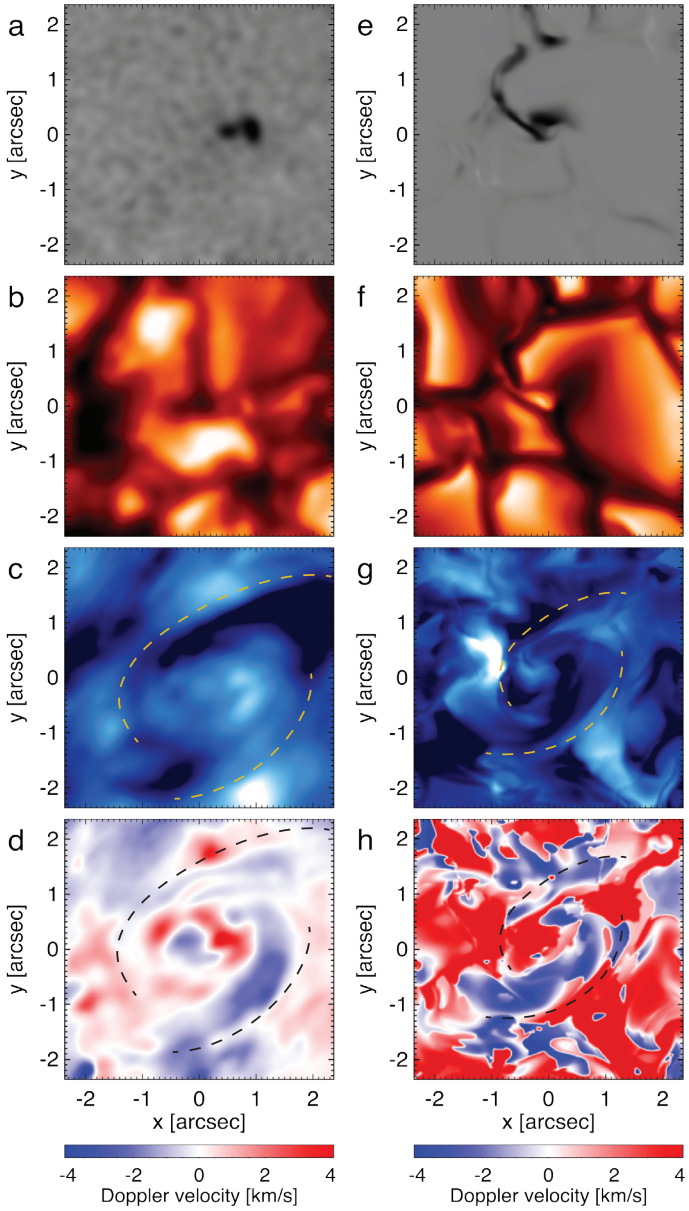

Supplementary Figure S2: Observational signature of chromospheric swirls. An observed swirl **(a-d)** is compared to a simulated swirl **(e-h)** from the same CO^{5}BOLD[21] model as in Fig. 3. The comparison includes magnetograms at the bottom of the photosphere, i.e. the visible 'surface' of the Sun **(a, e)**, the wide-band intensity **(b, f)**, the core of the spectral line of singly ionized calcium at 854 nm **(c, g),** and the corresponding Doppler shift of the line core wavelength **(d, h)**. The observation was carried out with the CRISP (CRisp Imaging Spectro-Polarimeter) instrument at the 1-m Swedish Solar Telescope on La Palma, Canary Islands, Spain (Scharmer, G. Comments

on the optimization of high resolution Fabry-Pérot filtergraphs. *Astron. Astrophys.* **447**, 1111, 2006). The CRISP/SST observations were processed with MOMFBD (Multi-Object Multi-Frame Blind Deconvolution) image restoration techniques (van Noort, M., Rouppe van der Voort, L., & Löfdahl, M. Solar Image Restoration By Use Of Multi-frame Blind De-convolution With Multiple Objects And Phase Diversity. *Sol. Phys.* **228**, 191, 2005). We used the radiative transfer program MULTI_3D (Carlsson, M. A Computer Program for Solving Multi-Level Non-LTE Radiative Transfer Problems in Moving or Static Atmospheres. Uppsala Astronomical Observatory: Report No. 33, 1986) to compute how the simulated swirl would be observed in the 854 nm infrared spectral line of Ca II **(g-h)**. The synthetic magnetogram **(e)** was computed with the full-Stokes radiative transfer code NICOLE (Socas-Navarro, H., de la Cruz Rodríguez, J., Asensio Ramos, A., Trujillo Bueno, J. & Ruiz Cobo, B. In prep.). The observed images appear more blurred owing to the limited spatial resolution. The observed properties of the swirls are reproduced well by the simulation. There is excellent agreement regarding the appearance of photospheric bright points in intergranular lanes **(a-b, e-f)**, the chromospheric pattern in the line core maps **(c, g)**, and also the Doppler shifts **(d, h)**. The successful reconstruction strongly suggests that chromospheric swirls are indeed the observational tracers of rotating magnetic flux structures.

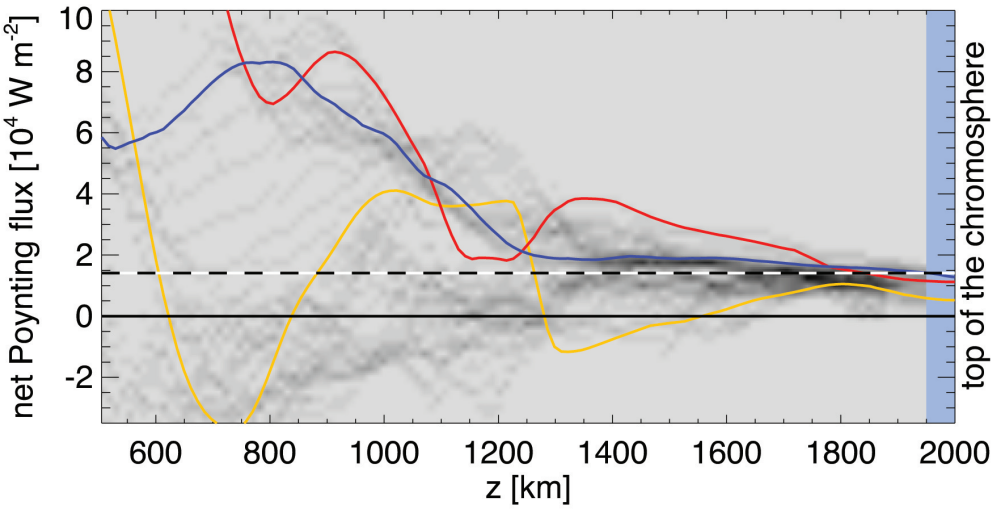

Supplementary Figure S3: Energy transport in small-scale magnetic tornadoes. The rotating magnetic field structure transports energy upwards to the top of the chromosphere. Within this swirling structure, there are regions with a large negative and regions with a large positive Poynting flux that cancel out except for a small residual. After a careful determination of the varying rotation axis and the boundaries of the swirling structure, the Poynting vector component parallel to the tilted axis is calculated. This parallel component, which is relevant for the energy transport, is averaged over the height-dependent area of the swirl (typically ≥ 2 Mm^2 in the upper layers). The resulting average is the remaining net flux, which is shown as function of height for three different time steps (coloured lines). All other time steps are visualised in form of a density map (grey scales in the background). The net flux is typically declining with height, an average of 1.4×10^4 W m^{-2} (dashed line) remains at the top of the model, which corresponds to the transition region at the boundary to the low corona in the Sun. A part of the remaining net flux of 1.4×10^4 W m^{-2} can be dissipated in the low corona, where it contributes significantly to the heating of the outer layers.

Supplementary Notes: Determination of the averaged net Poynting flux

For the analysed swirl in the CO^{5}BOLD simulation (see Fig. 3), we determine a net Poynting flux of

$$P_{sw} = 1.4 \times 10^4 \text{ W m}^{-2}$$

at the top of the model, which corresponds to the interface between the chromosphere and the corona (see Supplementary Figure 3).

With the conservative assumption that only an area of 2 Mm^2 inside the swirl is effectively contributing to the net Poynting flux, the net average Poynting flux over the area of the computational box of 8 Mm × 8 Mm is

$$P_{avg} = 440 \text{ W m}^{-2}.$$

The other 11 swirls, which we find in the same simulation sequence, are smaller and less pronounced but nevertheless could produce an additional contribution to the average Poynting flux.

Next we use the observations of May 8th, 2011 for an estimate of the average flux. Assuming that the simulation-based net Poynting flux of 1.4×10^4 W m^{-2} is delivered over an effective area of 6.6 Mm^2 (corresponding to the average swirl diameter of 4 arcsec), results in a total Poynting flux of 9.2×10^{16} W for each swirl. With 3.8 swirls being present in an area of 1 arcmin^2 at any instance in time, the resulting net average Poynting flux would be $(P_{avg})_{min} = 190$ W m^{-2}. This number presents a lower limit since the true number of swirls might be underestimated due to instrumental limitations.

Finally, we derive an upper limit based on the observed number densities of photospheric vortex flows[10] of 3×10^{-3} Mm^{-2} min^{-1}. With a vortex lifetime of 7.9 min[10], we conclude that 2.4×10^{-2} Mm^{-2} photospheric vortex flows are present at any instance in time. A net Poynting flux of 1.4×10^4 W m^{-2} over a large swirl area of 6.6

Mm^2 produces then an average flux of $(P_{avg})_{max}$ = 2,200 W m^{-2}. This number represents an upper limit since it is likely that not every photospheric vortex flow leads to the formation of a pronounced chromospheric swirl.

We conclude that the swirl simulation indicates an average Poynting flux of 440 W m^{-2}, which is well within the range of 190 W m^{-2} to up to 2,200 W m^{-2} as implied by the observations.